SCIENTIFIC REPORTS
nature research

OPEN

Dynamical Quantum Filtering via Enhanced Scattering of *para*-H_2 on the Orientationally Anisotropic Potential of $SrTiO_3$(001)

Koji Shimizu[1], Wilson Agerico Diño[1,2*], Hiroshi Nakanishi[1,3], Hideaki Kasai[1,3,4], Kotaro Takeyasu[4], Katsuyuki Fukutani[4] & Ayako Yajima[5]

Quantum dynamics calculation, performed on top of density functional theory (DFT)-based total energy calculations, show dynamical quantum filtering via enhanced scattering of *para*-H_2 on $SrTiO_3$(001). We attribute this to the strongly orientation-dependent (electrostatic) interaction potential between the H_2 (induced) quadrupole moment and the surface electric field gradient of ionic $SrTiO_3$(001). These results suggest that ionic surfaces could function as a scattering/filtering media to realize rotationally state-resolved H_2. This could find significant applications not only in H_2 storage and transport, but also in realizing materials with pre-determined characteristic properties.

The behavior/dynamics of H_2 on surfaces strongly depend on the H_2 molecular orientation/rotational states (rotational quantum number J, magnetic quantum number m) (cf., e.g., ref. [1] and references therein). On transition metal surfaces such as copper (Cu) and palladium (Pd), H_2 exhibits rotational alignment (cf., e.g., refs. [1,2] and references therein). One could then tune or design the structure of the metal (alloy) surfaces to dynamically filter the quantum rotational states of desorbing or scattered H_2 (dynamical quantum filtering), and control the H_2 dynamics (cf., e.g., refs. [1–7] and references therein). The resulting H_2 dynamics could, in turn, be used to probe local surface reactivity[8,9] (e.g., via the H_2(D_2) diffraction spectra[10–12]). On ionic crystal surfaces, the H_2 quadrupole moment interacts with the surface local electric field gradient to couple the translational and rotational degrees-of-freedom[13]. On $SrTiO_3$(001) (STO(001)), an ionic crystal material[14–21] with tunable surface terminations (cf., e.g., refs. [22,23]), H_2 adsorbs with the H-H bond oriented parallel (polar coordinate $\theta = \pi/2$) to the TiO_2-terminated surface at the Ti-site, and perpendicular ($\theta = 0$) to the SrO-terminated surface on top of the O-site (cf., Fig. 1)[24]. The strong orientationally anisotropic potential ($\Delta E^{\theta}_{\text{anisotropy}} = |E_{\theta=0} - E_{\theta=\pi/2}|$) results in adsorbed H_2 with (hindered) rotational states (J, m) different from that of gas phase H_2. These strongly hindered adsorption states lead to (J, m)-dependent thermal desorption energies[24–30], suggesting the possibility of separating para-H_2 [p-H_2($J = 0$, $m = 0$)] and ortho-H_2 [o-H_2($J = 1$, $m = \pm 1$)] through an adsorption-desorption process. This could find significant applications not only in H_2 storage and transport applications, but also in realizing materials with pre-determined characteristic properties.

As with metal (alloy) surfaces[5,8,9], the H_2 dynamics would be susceptible to the positive and negative charges that corrugate ionic crystal surfaces. In the following, we will show that on STO(001), under the influence of the orientationally anisotropic potential, on top of the surface lateral corrugation, p-H_2 scatter strongly at specific angles from the TiO_2-terminated and SrO-terminated STO(001). This dynamical filtering/scattering selectivity allows for more economical (less heat consumption) and more efficient means to rotationally separate o-H_2 and p-H_2, than the usual adsorption-desorption process[1–5,24–30].

Results and Discussion

H_2/$SrTiO_3$(001) System. Figure 1 shows a H_2 interacting with STO(001). X gives the surface lateral coordinate of the H_2 center-of-mass (CM) along the most corrugated directions on the two STO(001) terminations, viz., along [100] for TiO_2-termination (Ti-O-Ti row) and along [110] for SrO-termination (Sr-O-Sr row), respectively

[1]Department of Applied Physics, Osaka University, Osaka, 565-0871, Japan. [2]Center for Atomic and Molecular Technologies, Osaka University, Osaka, 565-0871, Japan. [3]National Institute of Technology, Akashi College, Hyogo, 674-8501, Japan. [4]Institute of Industrial Science, The University of Tokyo, Tokyo, 153-8505, Japan. [5]Kawasaki Heavy Industries, Ltd., Hyogo, 673-8666, Japan. *email: wilson@dyn.ap.eng.osaka-u.ac.jp

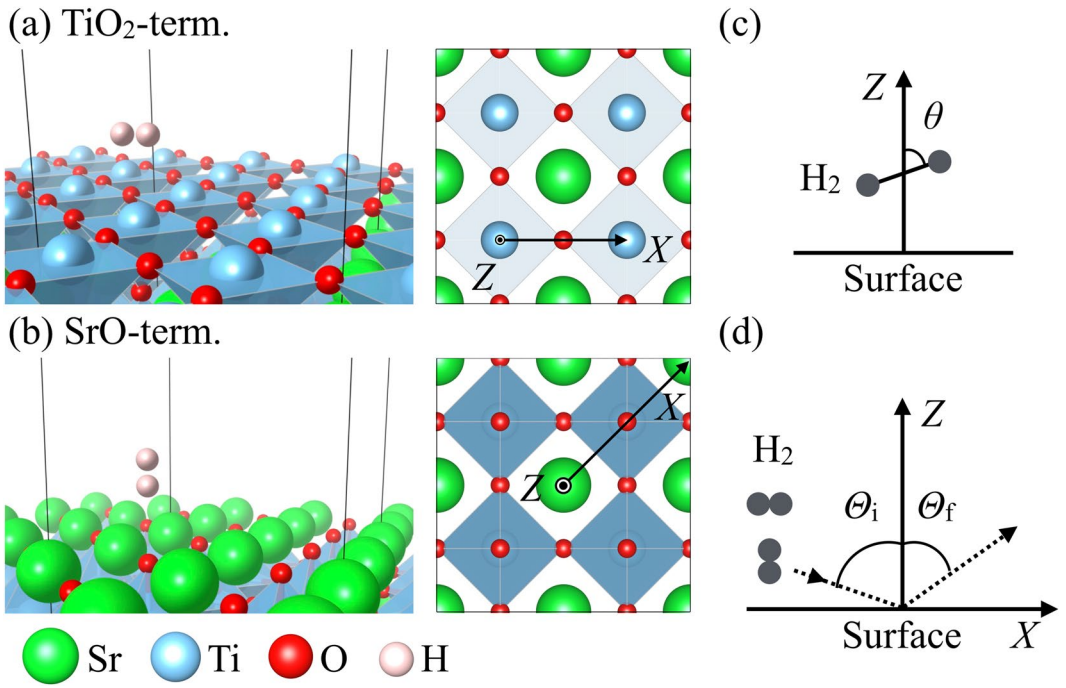

Figure 1. A depiction of H_2 adsorption (**a**) atop the Ti-site and (**b**) atop the O-site on the TiO_2- and SrO-terminated $SrTiO_3(001)$, with corresponding preferential orientations $\theta = \pi/2$ and 0, respectively. The lower left panel shows which colored balls correspond to which element. (**c**) A depiction of H_2 with the H_2 center-of-mass (CM) at a distance Z from the surface, and the H-H bond at an orientation θ with respect to the surface normal. (**d**) A depiction of H_2 scattering on $SrTiO_3(001)$ with angle of incidence Θ_i and scattering angle Θ_f. X corresponds to the surface lateral position of the H_2 CM along the (**a**) [100] and (**b**) [110] direction on the TiO_2- and SrO-terminated $SrTiO_3(001)$, respectively.

(cf., Fig. 1(a,b)). Z gives the normal distance of the H_2 CM from the surface. θ gives the polar angular orientation of the H-H bond with respect to the surface normal. ϕ (not shown) gives the azimuthal angular orientation of the H-H bond about the surface normal, with respect to the X-axis, at each site on STO(001). $\Theta_{i(f)}$ gives H_2 incidence (scattering) angle measured with respect to the surface normal (cf., Fig. 1(c,d)). In the following, given $H_2(J_i, m_i, E_i, \Theta_i)$, we determine the probability of finding $H_2(J_f, m_f, E_f, \Theta_f)$. $H_2(J_i, m_i, E_i, \Theta_i)$ indicates a H_2 with initial rotational state (J_i, m_i), impinging STO(001) with an initial incident translational energy E_i and at an incidence angle Θ_i with respect to the surface normal. $H_2(J_f, m_f, E_f, \Theta_f)$ indicates a H_2 with final rotational state (J_f, m_f), scattered from STO(001) with a final translational energy E_f and at a scattering angle Θ_f with respect to the surface normal.

Orientationally anisotropic electrostatic potential. In Figs. 2 and 3, we plot the (electrostatic interaction energies) dot products of the (induced) dipole moment with the surface electric field U_i and the (induced) quadrupole moment with the gradient of the surface electric field $V_{i,j}$, for the TiO_2-terminated and SrO-terminated surfaces, respectively. We can see that the orientational (θ) anisotropy $\Delta E^{\theta}_{\text{anisotropy}}$ becomes important when the impinging H_2 comes sufficiently near the surface, viz., at $Z \leq 2.4$ Å above the Ti-site and $Z \leq 2.6$ Å above the O-site on the TiO_2- and SrO-terminated surfaces, respectively. On the other hand, far from the surface, viz., at $Z \geq 3.2$ Å above the O-site and $Z \geq 3.0$ Å above the Sr-site of the TiO_2- and SrO-terminated surfaces, respectively, only a small $\Delta E^{\theta}_{\text{anisotropy}}$ can be observed. This orientational anisotropy $\Delta E^{\theta}_{\text{anisotropy}}$, on top of the surface lateral corrugation, would prove to be useful in our attempt to control the H_2 scattering dynamics, as we will discuss in detail in the next sections.

H_2 Scattering along STO(001)[100] on TiO_2-terminated STO(001). In Fig. 4(a–c), we show the calculated (scattering) probabilities/spectra $P^{m_i \to m_f}_{J_i \to J_f}(E_i = 80\text{ meV}, E_f, \Theta_i = 15.9°, \Theta_f)$ of finding $H_2(J_i, m_i, E_i = 80\text{ meV}, \Theta_i = 15.9°)$ scattered as $H_2(J_f, m_f, E_f, \Theta_f)$ along the [100] direction of a TiO_2-terminated STO(001). (The corresponding initial surface perpendicular translational energy $E_i \times \cos^2\Theta_i = 80\text{ meV} \times \cos^2(15.9°) \sim 74.0$ meV and initial surface lateral translational energy $E_i \times \sin^2\Theta_i = 80\text{ meV} \times \sin^2(15.9°) \sim 6.00$ meV). This corresponds to the maximum p-H_2 to o-H_2 ratio $R_{J=0/J=1}(E_i = 80\text{ meV}, \Theta_i = 15.9°, \Theta_f)$ on a TiO_2-terminated STO(001) (cf., Table 1). The resulting trends can be explained by inspecting the corresponding orientational anisotropy and surface lateral corrugation of the potential encountered by the impinging $H_2(J_i, m_i, E_i = 80\text{ meV}, \Theta_i = 15.9°)$ (i.e., $\langle Y^m_J | V(Z, \theta, X) | Y^m_J \rangle$, cf., Fig. 4(d)). Note that along STO(001)[100], $H_2(J_i = 0, m_i = 0)$ encounters a strongly corrugated and orientationally anisotropic PES (cf., solid curve in Fig. 4(d)), that favors molecular

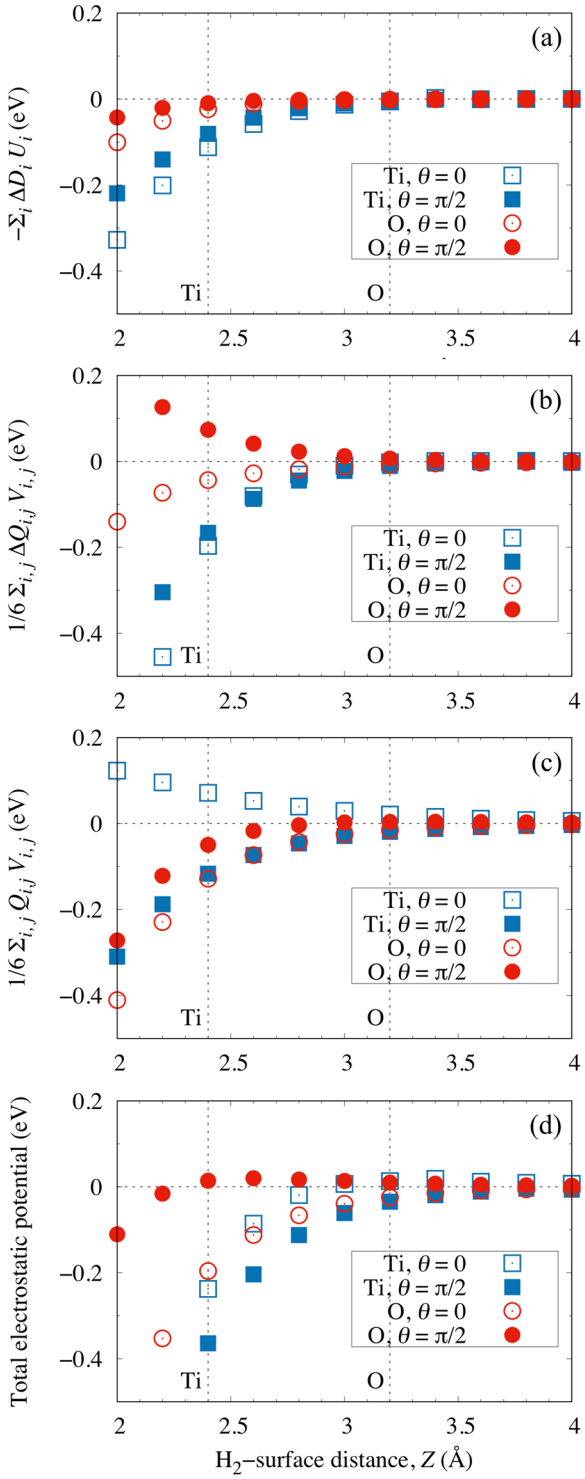

Figure 2. Calculated electrostatic potential contributions from (**a**) the induced dipole moment ΔD_i with the surface electric field U_i, (**b**) the induced quadrupole moment $\Delta Q_{i,j}$ and (**c**) the H_2 quadrupole moment $Q_{i,j}$ with the gradient of the surface electric field $V_{i,j}$, on the Ti-site (squares) and the O-site (circles) with $\theta = 0$ (open symbols) and $\theta = \pi/2$ (filled symbols) for the TiO_2-terminated STO(001). (**d**) The sum of the contributions (**a**–**c**). $i, j = (x, y, z)$. The dotted vertical lines intercepting the abscissas indicate locations of the corresponding potential energy minima (H_2-surface equilibrium distance) at each respective surface site.

adsorption atop the Ti-site, with H-H bond oriented parallel to the surface, and an adsorption energy $E_{ads} = -191$ meV[24]. Atop the O-site, H_2 preferentially adsorbs with the H-H bond oriented perpendicular to the surface, with $E_{ads} = -72.5$ meV[24]. As a result, in Fig. 4(a), we find a corresponding spectra dominated by off-specularly scattered H_2, with dominant components coming from backscattering. Most of the $H_2(J_i = 0, m_i = 0)$ would be

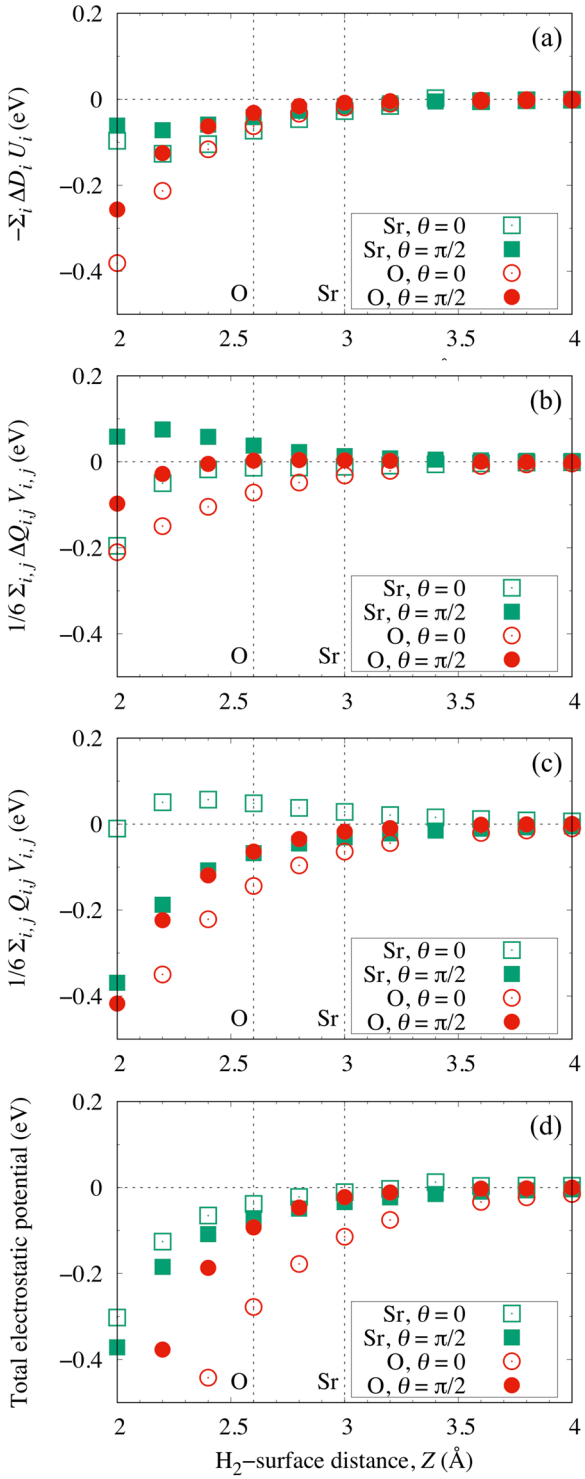

Figure 3. Calculated electrostatic potential contributions from (**a**) the induced dipole moment ΔD_i with the surface electric field U_i, (**b**) the induced quadrupole moment $\Delta Q_{i,j}$ and (**c**) the H_2 quadrupole moment $Q_{i,j}$ with the gradient of the surface electric field $V_{i,j}$, on the Sr-site (squares) and the O-site (circles) with $\theta = 0$ (open symbols) and $\theta = \pi/2$ (filled symbols) for the SrO-terminated STO(001). (**d**) The sum of the contributions (**a**–**c**). $i, j = (x, y, z)$. The dotted vertical lines intercepting the abscissas indicate the locations of the corresponding potential energy minima (H_2-surface equilibrium distance) at each respective surface site.

molecularly adsorbed (due to *reorientation/steering*[31,32]), and only a small fraction would be elastically scattered (due to *shadow effect*[9]). Considering the angle of incidence, the inelastically scattered H_2 would come from those hitting the repulsive part of the potential well near the O-site (*shadow effect*, cf., solid curve in Fig. 4(d)), resulting in a change in surface lateral momentum and off-specular scattering angles. Energy transfer from the

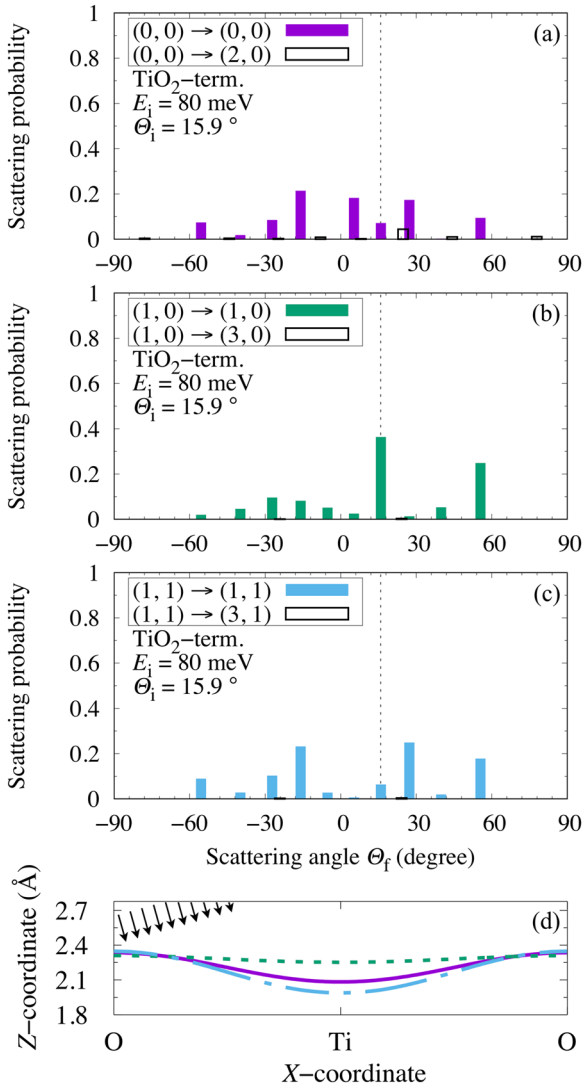

Figure 4. (**a**–**c**) Calculated H_2 scattering probability $(J_i, |m_i|) \rightarrow (J_f, |m_f|)$ from initial rotational state $(J_i, |m_i|)$ to final rotational state $(J_f, |m_f|)$ on the TiO_2-terminated STO(001) as a function of the scattering angle Θ_f, for incident energy $E_i = 80$ meV and incident angle $\Theta_i = 15.9°$. The dotted vertical lines intercepting the abscissas indicate specular scattering. (**d**) Solid, dotted, and dash-dot lines indicate constant energy surfaces of $\langle Y_J^m | V(Z, \theta, X) | Y_J^m \rangle$ (with 80 [meV] $\times \cos^2\Theta_i$: corresponding to H_2 surface normal translational energy) encountered by a H_2 impinging with initial rotational states (J_i, m_i): [(0, 0), (1, 0), (1, 1)], respectively. Same scales used for X- and Z-coordinates. The arrows indicate the direction of incidence of the impinging H_2.

E_i [meV]	Θ_i[°]	Θ_f[°]	$R_{J=0/J=1}$	$\overline{R_{J=0/J=1}}$
10.0	15.0	15.0	1.45	0.470
20.0	47.1	0.00	1.91	0.155
30.0	48.4	48.4	1.14	0.397
40.0	40.4	−7.44	1.92	0.0967
50.0	20.3	6.65	2.65	0.449
60.0	18.5	31.9	1.70	0.0753
70.0	43.3	43.3	1.64	0.265
80.0	15.9	5.26	4.96	0.271

Table 1. Calculated $R_{J=0/J=1}(E_i, \Theta_i, \Theta_f)$ and $\overline{R_{J=0/J=1}}(E_i, \Theta_i, \Theta_f)$ on TiO_2-terminated STO(001) at the incident energy range 10 meV $\leq E_i \leq$ 80 meV. For each incident energy, we list only the maximum $R_{J=0/J=1}(E_i, \Theta_i, \Theta_f)$ with the corresponding incident and scattering angles.

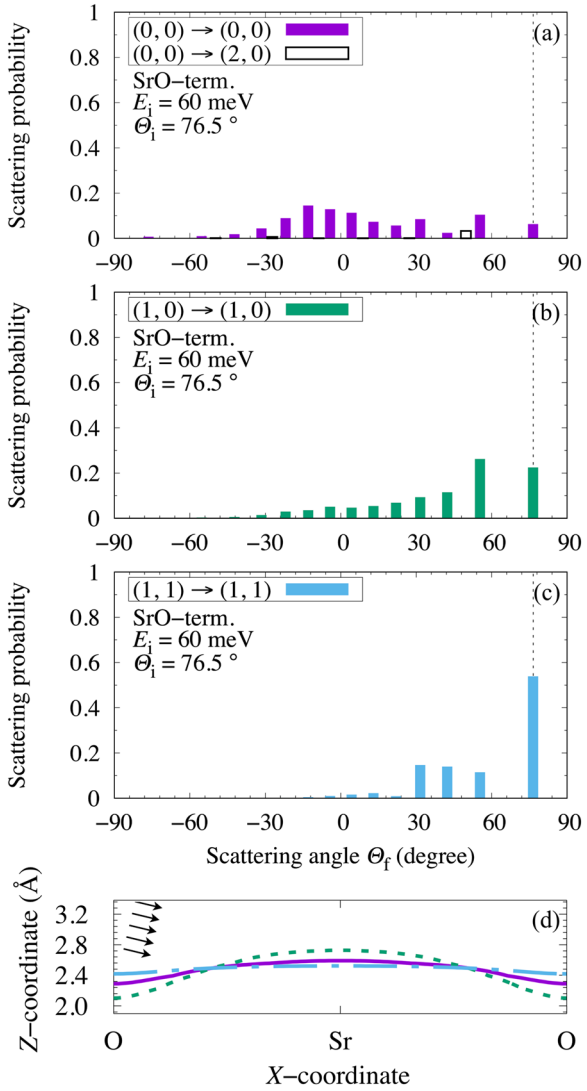

Figure 5. (**a**–**c**) Calculated H_2 scattering probability $(J_i, |m_i|) \rightarrow (J_f, |m_f|)$ from initial rotational state $(J_i, |m_i|)$ to final rotational state $(J_f, |m_f|)$ on the SrO-terminated STO(001) as a function of the scattering angle Θ_f, for incident energy $E_i = 60$ meV and incident angle $\Theta_i = 76.5°$. The dotted vertical lines intercepting the abscissas indicate specular scattering. (**d**) Solid, dotted, and dash-dot lines indicate constant energy surfaces of $\langle Y_J^m | V(Z, \theta, X) | Y_J^m \rangle$ (with 60 [meV] $\times \cos^2\Theta_i$: corresponding to H_2 surface normal translational energy) encountered by a H_2 impinging with initial rotational states (J_i, m_i): [(0, 0), (1, 0), (1, 1)], respectively. Same scales used for *X*- and *Z*-coordinates. The arrows indicate the direction of incidence of the impinging H_2.

translational degree-of-freedom (DOF) to the rotational DOF allows the molecule more time to sample the anisotropic surface through *reorientation/steering*. Those that succeed would molecularly adsorb. Those that fail, would be rotationally de-excited on the way back to the gas phase, because of the smaller anisotropic potential further (out in the vacuum) from the surface. Thus, the scattering spectra shows negligible rotationally excited H_2, i.e., $H_2(J_f = 2, m_i = 0)$. $H_2(J_i = 1, m_i = \pm 1)$ also encounters a strongly anisotropic PES (cf., dash-dot curve in Fig. 4(d)). Thus, we see the same trend in Fig. 4(c), i.e., a corresponding spectra dominated by off-specularly scattered H_2, with dominant components coming from backscattering. On the other hand, $H_2(J_i = 1, m_i = 0)$ encounters an almost flat PES (cf., dotted curve in Fig. 4(b)). As a result, we see strong (dominant) specular scattering of $H_2(J_i = 1, m_i = 0)$ (Fig. 4(b)). Finally, we could observe a *p*-H_2 to *o*-H_2 ratio as large as ca. 4.96 (cf., Table 1) compared to that of *normal*-H_2 (*n*-H_2) (i.e., >1/3 at 300 K) at scattering angle $\Theta_f = 5.26°$ (Fig. 4).

H_2 Scattering along STO(001)[110] on SrO-terminated STO(001). In Fig. 5(a–c), we show the calculated (scattering) probabilities/spectra corresponding to the maximum *para*-to-*ortho* ratio $R_{J=0/J=1}(E_i = 60$ meV, $\Theta_i = 76.5°, \Theta_f)$, along the [110] direction of a SrO-terminated STO(001) (cf., Table 2). (The initial surface perpendicular translational energy $E_i \times \cos^2\Theta_i = 60$ meV $\times \cos^2(76.5°) \sim 3.27$ meV and the initial surface lateral translational energy $E_i \times \sin^2\Theta_i = 60$ meV $\times \sin^2(76.5°) \sim 56.7$ meV.) Again, the resulting trends can be explained by inspecting the corresponding orientational anisotropy and surface lateral corrugation of the

E_i[meV]	Θ_i[°]	Θ_f[°]	$R_{J=0/J=1}$	$\overline{R_{J=0/J=1}}$
10.0	0.00	47.1	1.32	0.124
20.0	7.44	22.9	5.97	0.496
30.0	47.8	−47.8	11.4	0.529
40.0	15.9	−55.5	4.06	0.137
50.0	47.5	47.5	2.90	0.541
60.0	76.5	−76.5	16.1	0.0294
70.0	7.96	56.2	1.57	0.0194
80.0	57.3	−57.3	1.73	0.00328

Table 2. Calculated $R_{J=0/J=1}(E_i, \Theta_i, \Theta_f)$ and $\overline{R_{J=0/J=1}}(E_i, \Theta_i, \Theta_f)$ on SrO-terminated STO(001) at the incident energy range 10 meV $\leq E_i \leq$ 80 meV. For each incident energy, we list only the maximum $R_{J=0/J=1}(E_i, \Theta_i, \Theta_f)$ with the corresponding incident and scattering angles.

potential encountered by the impinging $H_2(J_i, m_i, E_i = 60\,\text{meV}, \Theta_i = 76.5°)$ (i.e., $\langle Y_J^m|V(Z, \theta, X)|Y_J^m\rangle$, cf., Fig. 5(d)). Note that along STO(001)[110] on the SrO-terminated STO(001), $H_2(J_i = 0, m_i = 0)$ encounters a strongly corrugated and orientationally anisotropic PES (cf., solid curve in Fig. 5(d)), that now favors molecular adsorption atop the O-site, with H-H bond oriented perpendicular to the surface, and an adsorption energy $E_{ads} = -151$ meV[24]. Atop the Sr-site, H_2 adsorbs with the H-H bond oriented parallel to the surface, and $E_{ads} = -111$ meV[24]. As a result, in Fig. 5(a), we find a corresponding spectra dominated by off-specularly scattered H_2, with dominant components coming from backscattering. Again, most of the $H_2(J_i = 0, m_i = 0)$ would be molecularly adsorbed (due to *reorientation/steering*[31,32]), and only a small fraction would be elastically scattered (possibly due to *shadow effect*[9]). Considering the angle of incidence, the inelastically scattered H_2 would come from those hitting the repulsive part of the potential well near the Sr-site (*shadowing effect*, cf., solid curve in Fig. 4(d)), resulting in a change in surface lateral momentum and off-specular scattering angles. Note that the impinging H_2 has a larger surface lateral momentum as compared to the corresponding surface perpendicular component. This allows the impinging H_2 more time to explore the anisotropic surface. Those that succeed would molecularly adsorb via *reorientation/steering*. Those that fail, would be rotationally de-excited on the way back to the gas phase, because of the smaller anisotropic potential further (out in the vacuum) from the surface. Thus, the scattering spectra shows negligible rotationally excited H_2, i.e., $H_2(J_f = 2, m_i = 0)$. $H_2(J_i = 1, m_i = \pm 1)$ also encounters a strongly anisotropic PES (cf., dash-dot curve in Fig. 5(d)). But now recall that the preferred adsorption site is at the O-site, with the H-H bond oriented perpendicular to the surface. Thus, we see strong specular scattering in Fig. 5(c). $H_2(J_i = 1, m_i = 0)$ shows higher backscattering probabilities (cf., Fig. 5(b)) due to the larger surface anisotropy along X, making it more susceptible to reorientation/steering. Finally, we could observe a p-H_2 to o-H_2 ratio as large as ca. 16.1 (cf., Table 2) compared to that of n-H_2 (i.e., >1/3 at 300 K) at scattering angle $\Theta_f = -76.5°$ (Fig. 5).

(Normalized) p-H_2 to o-H_2 Ratios. In Tables 1 and 2, we show the calculated p-H_2 to o-H_2 ratio $R_{J=0/J=1}(E_i, \Theta_i, \Theta_f)$ and the normalized p-H_2 to o-H_2 ratio $\overline{R_{J=0/J=1}}(E_i, \Theta_i, \Theta_f)$ of H_2 scattered from the TiO_2-terminated and SrO-terminated STO(001), respectively. The incident energy ranges from 10 meV $\leq E_i \leq$ 80 meV. Assuming Maxwell-Boltzmann distribution, at 300 K, 90% of the impinging H_2 would have kinetic energies less than 80 meV. In general, the SrO-terminated STO(001) show a much higher p-H_2 yield compared to the TiO_2-terminated STO(001). On TiO_2-terminated STO(001), we observe a maximum p-H_2 to o-H_2 ratio of $R^{max}_{J=0/J=1} = 4.96$ for $E_i = 80.0$ meV, $\Theta_i = 15.9°$, $\Theta_f = 5.26°$. Whereas on SrO-terminated STO(001), we observe a maximum p-H_2 to o-H_2 ratio of $R^{max}_{J=0/J=1} = 16.1$ for $E_i = 60$ meV, $\Theta_i = 76.5°$, $\Theta_f = -76.5°$. The results suggest that, for all incident energies E_i considered, the p-H_2 to o-H_2 ratios at specific scattering angles Θ_f exceed that of n-H_2, i.e., $R_{J=0/J=1}(E_i, \Theta_i, \Theta_f) > 1/3$, at room temperature ($T = 300$ K).

Conclusion

Here, we reported increased *para*-H_2 (p-H_2) to *ortho*-H_2 (o-H_2) ratio of H_2 scattered from $SrTiO_3$(001) (viz., ca. 4.96 and 16.1 along the $SrTiO_3$(001)[100] and $SrTiO_3$(001)[110] of the TiO_2- and SrO-terminated $SrTiO_3$(001), respectively). For reference, *normal*-H_2 (n-H_2) have a p-H_2 to o-H_2 ratio of 1/3, at room temperature ($T = 300$ K). We attribute this to the strongly orientation-dependent (electrostatic) interaction potential between the H_2 (induced) quadrupole moment and the surface electric field of ionic $SrTiO_3$(001). These results suggest that ionic surfaces (with tunable surface terminations) could function as a scattering/filtering media to realize rotationally state-resolved H_2. This could find significant applications not only in H_2 storage and transport, but also in realizing materials with pre-determined characteristic properties.

We can compare the present results to previous reports for the inelastic scattering of H_2 on LiF(001), at normal incidence ($\Theta_i = 0°$) and incident energy of $E_i = 100$ meV[33]. From the scattering probability data[33], we estimate a maximum p-H_2 to o-H_2 ratio $R_{J=0/J=1}$ of ca. 2 (as compared to ca. 4.96 and 16.1 along $SrTiO_3$(001)[100] and $SrTiO_3$(001)[110] of the TiO_2- and SrO-terminated $SrTiO_3$(001), respectively). (Note that the results of ref. [33] have since been confirmed experimentally[34]).

Considering the Debye temperature of $SrTiO_3$ (ca. 413.3 K[35]), we may expect some thermal modulation/attenuation. With Ti having a smaller mass than Sr, we would expect more pronounced effect (modulation/attenuation) on TiO_2-terminated $SrTiO_3$(001), as compared to SrO-terminated $SrTiO_3$(001). Consider for example a

surface temperature of 100 K and incidence angle Θ_i: [0°, 66°]. For TiO_2-terminated $SrTiO_3(001)$, we estimated Debye-Waller factor values (cf., e.g., ref. [12] for more details) ranging from ca. 0.3 to 0.6, increasing with increasing incidence angle Θ_i. In comparison, for SrO-terminated $SrTiO_3(001)$, we estimated[12] Debye-Waller factor values ranging from ca. 0.6 to 0.8, increasing in value with increasing incidence angle Θ_i. The modulation/attenuation would become more pronounced with increased temperature. However, regardless of the degree of modulation/attenuation, the maximum p-H_2 to o-H_2 ratio for each surface termination remained almost the same (viz., ca. 4.48 and 16.7 along the $SrTiO_3(001)[100]$ and $SrTiO_3(001)[110]$ of the TiO_2- and SrO-terminated $SrTiO_3(001)$, respectively, at 100 K).

Finally, because of the wide spread of the scattering angle, we could expect small scattering probabilities at each particular scattering angle. Furthermore, the larger the (surface lateral) incident energy, the more number of (surface lateral) diffraction channels (would be) involved (excited). As a result, the normalized p-H_2 to o-H_2 ratio $R_{J=0/J=1}$ shows small values (cf., Tables 1 and 2). Thus, so far, we can collect only a small amount of H_2 through any given scattering event. (But with high purity!) For engineering applications, scattering at optimum surface angles should resolve this problem.

Methods

Model Hamiltonian. To study the dynamics of H_2 scattering on STO(001) (Fig. 1), we performed quantum dynamical calculations (cf., e.g., refs. [1–5,8,9,24,31,32]) by solving the corresponding time-independent Schrödinger equation for H_2, in the vibrational ground state ($\nu = 0$), under the influence of an orientationally anisotropic potential energy (hyper-) surface (PES), using the coupled-channel method[36–42]. The dynamical variables we considered include the H_2 center-of-mass (CM) distance Z from the surface, the H_2 bond-length r, the polar and azimuthal angular orientations of the H-H bond with respect to the surface, θ and ϕ, respectively, and the position of the H_2 CM X, along STO(001)[100] and STO(001)[110] of the TiO_2- and SrO-terminated STO(001), respectively. Considering that the energy scale of the H_2 molecular vibration ($\hbar\omega = 516$ meV) exceeds the energy range relevant to our current study (i.e., E_i: [10, 80] meV), we can neglect the molecular vibrational excitations, and fix the H_2 interatomic distance at $r = 0.74$ Å. The small variation of the potential energy with respect to ϕ allows us to further neglect the ϕ-dependence[24]. Thus, we can reduce the original 6-Dimensional (6-D) Hamiltonian (for the diatomic molecule-surface system) to the following simplified 3-D form :

$$H = -\frac{\hbar^2}{2m}\left(\frac{\partial^2}{\partial Z^2} + \frac{\partial^2}{\partial X^2}\right) - \frac{\hbar^2}{2I}\left[\frac{1}{\sin\theta}\frac{\partial}{\partial\theta}\left(\sin\theta\frac{\partial}{\partial\theta}\right) + \frac{1}{\sin^2\theta}\frac{\partial^2}{\partial\phi^2}\right] + V(Z, \theta, X). \tag{1}$$

m and I correspond to the H_2 total mass and moment of inertia, respectively.

Potential Energy (Hyper-) Surface: PES. The 3-D PES $V(Z, \theta, X)$ in Eq. (1) comes from previously performed density functional theory (DFT)-based total energy calculations[43–45] for H_2 adsorption at the Ti and O surface sites on the TiO_2-terminated STO(001), the Sr and O surface sites on the SrO-terminated STO(001), and H_2 polar orientations $\theta = 0$ and $\pi/2$[24]. We fitted the potential energy curves for each configuration using Morse potentials:

$$V_{A(B),\theta} = D_{A(B),\theta} \times \{\exp[-2\alpha_{A(B),\theta}(Z - Z^{eq}_{A(B),\theta})] - 2\exp[\alpha_{A(B),\theta}(Z - Z^{eq}_{A(B),\theta})]\}, \tag{2}$$

and connected the Morse potentials for $\theta = 0$ and $\pi/2$ at each surface site and for different surface sites to get

$$V(Z, \theta, X) = [V_{A,\theta=\pi/2}\sin^2\theta + V_{A,\theta=0}\cos^2\theta]\cos^2 gX + [V_{B,\theta=\pi/2}\sin^2\theta + V_{B,\theta=0}\cos^2\theta]\sin^2 gX. \tag{3}$$

$D_{A(B),\theta}$, $\alpha_{A(B),\theta}$, $Z^{eq}_{A(B),\theta}$ give the corresponding potential depth, potential width, and equilibrium (normal/perpendicular) distance of H_2 from the surface cation sites (A:[Ti, Sr]) and oxygen site (B), at H-H bond angle θ, respectively. The reciprocal lattice constant $g_X (= \pi/a_X)$, with corresponding direct lattice constants $a_X^{[100]} = 3.91$ Å and $a_X^{[110]} = 5.52$ Å along [100] and [110] of the TiO_2- and SrO-terminated STO(001), respectively[46]. Table 3 shows the fitted parameters for each configuration. We used spherical harmonics and plane waves as basis sets for the rotational motion and the translational motion (perpendicular to the surface and along the surface direction X), respectively.

To extract the contribution of the electrostatic interaction between the H_2 quadrupole moment and the surface local electric field, as discussed above, we used the charge density distribution obtained from previous DFT-based total energy calculations[24]. We calculated the induced dipole ΔD_i ($i = x, y, z$) and quadrupole moments $\Delta Q_{i,j}$ ($i, j = x, y, z$) from the charge density difference ($\Delta\rho(Z) = \rho_{H_2/STO}(Z) - \rho_{H_2} - \rho_{STO}$) as a function of Z for the Ti and O sites (TiO_2-termination) and Sr and O sites (SrO-termination) with $\theta = 0$ and $\pi/2$. We also calculated the H_2 quadrupole moment $Q_{i,j}$ from the charge density distribution of the isolated system. We used the pristine STO(001) to calculate the surface electric field and its gradient.

Scattering probability. Consider a H_2 impinging with an initial rotational state (J_i, m_i), incident energy E_i, and angle of incidence with respect to the surface normal Θ_i (cf., e.g., Fig. 1(c,d), and Table 4). Using the coupled-channel method[36–42], we calculated the probability $P^{m_i\to m_f}_{J_i\to J_f}(E_i, E_f, \Theta_i, \Theta_f)$ of finding the H_2 scattered with a final rotational state (J_f, m_f), final kinetic energy E_f, scattering at an angle of Θ_f with respect to the surface normal. (We carefully checked the convergence for calculations with maximum quantum numbers $J_{max} = 10$ and $|G_{X_{max}}| = 30$). From the calculated scattering probability $P^{m_i\to m_f}_{J_i\to J_f}(E_i, E_f, \Theta_i, \Theta_f)$ of H_2 on STO(001), we evaluated

Surface	adsorption	θ	D	α	Z^{eq}
Termination	site	[rad]	[eV]	[Å^{-1}]	[Å]
TiO_2	Ti site-A	0	0.0390	1.40	3.18
		$\pi/2$	0.172	1.47	2.37
	O site-B	0	0.0665	1.30	2.97
		$\pi/2$	0.0486	1.24	3.14
	Sr site-A	0	0.0409	1.21	3.57
SrO		$\pi/2$	0.108	1.39	2.93
	O site-B	0	0.152	1.18	2.55
		$\pi/2$	0.0322	0.755	3.70

Table 3. Fitted values of the potential depth D, potential width α, and equilibrium distance from the surface Z^{eq}, at each surface site, in Eq. (3).

	TiO_2-termination	SrO-termination
	$a_X^{[100]} = 3.91$ Å	$a_X^{[110]} = 5.52$ Å
	$E_i = 80$ meV	$E_i = 60$ meV
	$E_i^{total}(J=0) = 80.0$ meV	$E_{total}(J=0) = 60.0$ meV
	$E_i^{total}(J=1) = 95.2$ meV	$E_{total}(J=1) = 75.2$ meV
G_{i_X}	incident angle Θ_i[°]	incident angle Θ_i [°]
0	0.00	0.00
1	5.26	4.29
2	10.6	8.60
3	15.9†	13.0
4	21.5	17.4
5	27.3	22.0
6	33.3	26.7
7	39.9	31.6
8	47.1	36.7
9	55.5	42.3
10	66.3	48.4
11	—	55.3
12	—	63.8
13	—	76.5‡

Table 4. Some relevant physical values corresponding to $H_2(E_i, J_i, m_i, \Theta_i)$ impinging a TiO_2- and SrO-terminated $SrTiO_3(001)$. Incident angles presented in this work doubly underlined. $^{\dagger}E_{\parallel} = E_X = E_i\sin^2 15.9^\circ \sim 6.004$ meV. $^{\dagger}E_{\perp} = E_Z = E_i\cos^2 15.9^\circ \sim 74.00$ meV. $^{\ddagger}E_{\parallel} = E_X = E_i\sin^2 76.5^\circ \sim 56.73$ meV. $^{\ddagger}E_{\perp} = E_Z = E_i\cos^2 76.5^\circ \sim 3.270$ meV. • E_i: incident energy. • (J_i, m_i): initial rotational state. • Θ_i: incident angle with respect to the surface normal. • $E_i^{total} = E_i + E_{J_i}$: total initial kinetic energy. • $E_{J_i} = B_{H_2}J_i(J_i+1)$: initial rotational energy. • $B_{H_2} = 7.6$ meV: H_2 rotational constant. • $E_\perp = E_Z = E_i\cos^2\Theta$: surface normal translational energy. • $E_\parallel = E_X = E_i\sin^2\Theta = \frac{\hbar^2}{2M}\left[gG_{i_X}\right]^2$: surface lateral translational energy. • M: H_2 total mass. • $g = \frac{\pi}{a_X}$: reciprocal lattice constant. • a_X: direct lattice constant. • G_{i_X}: surface lateral wave number (integer).

the corresponding p-H_2 to o-H_2 ratio $R_{p-H_2(J=0)/o-H_2(J=1)}(E_i, \Theta_i, \Theta_f) = R_{J=0/J=1}(E_i, \Theta_i, \Theta_f)$, given the incident energy E_i, incident angle Θ_i, and scattering angle Θ_f, i.e.,

$$R_{J=0/J=1}(E_i, \Theta_i, \Theta_f) = \frac{\int dE_f\, P^{m_i=0\to m_f=0}_{J_i=0\to J_f=0}(E_i, E_f, \Theta_i, \Theta_f)}{\int dE_f \sum_{m=-1}^{1} P^{m_i\to m_f=m_i}_{J_i=1\to J_f=1}(E_i, E_f, \Theta_i, \Theta_f)} = \frac{P_0^0(E_i, \Theta_i, \Theta_f)}{\sum_{m=-1}^{1} P_1^m(E_i, \Theta_i, \Theta_f)}. \tag{4}$$

Note that

$$\int dE_f \sum_{J_f, m_f, \Theta_f} P^{m_i\to m_f}_{J_i\to J_f}(E_i, E_f, \Theta_i, \Theta_f) = 1. \tag{5}$$

And since we are considering the case when $J_i = J_f$ and $m_i = m_f$, in Eq. (4) we have

$$P^{m_i\to m_f}_{J_i\to J_f}(E_i, E_f, \Theta_i, \Theta_f) = P^{m_i\to m_{f=i}}_{J_i\to J_{f=i}}(E_i, E_f, \Theta_i, \Theta_f) = P^m_J(E_i, \Theta_i, \Theta_f). \tag{6}$$

We also calculated the normalized p-H_2 to o-H_2 ratio $\overline{R_{J=0/J=1}}(E_i, \Theta_i, \Theta_f)$, i.e.,

$$\overline{R_{J=0/J=1}}(E_i, \Theta_i, \Theta_f) = R_{J=0/J=1}(E_i, \Theta_i, \Theta_f) \times \frac{P_0^0(E_i, \Theta_i, \Theta_f) + \sum_{m=-1}^{1} P_1^m(E_i, \Theta_i, \Theta_f)}{\sum_{\Theta_f=-90^\circ}^{90^\circ}[P_0^0(E_i, \Theta_i, \Theta_f) + \sum_{m=-1}^{1} P_1^m(E_i, \Theta_i, \Theta_f)]}. \quad (7)$$

In Eq. (7), we multiplied the angle specific p-H_2 to o-H_2 ratio by a normalization factor, so as to evaluate the efficiency of rotational state separation with respect to the incident n-H_2. Note that the p-H_2 to o-H_2 ratio of n-H_2 corresponds to 0.333 (1/3) at room temperature ($T = 300$ K)

Received: 14 January 2020; Accepted: 17 March 2020;
Published online: 03 April 2020

References

1. Diño, W. A., Kasai, H. & Okiji, A. Orientational effects in dissociative adsorption/associative desorption dynamics of H_2 (D_2) on Cu and Pd. *Prog. Surf. Sci.* **63**, 63–134 (2000).
2. Diño, W. A., Kasai, H. & Okiji, A. Rotational Alignment in the Associative Desorption Dynamics of Hydrogen Molecules from Metal Surfaces. *J. Phys. Soc. Jpn.* **67**, 1517–1520 (1998).
3. Diño, W. A., Kasai, H. & Okiji, A. Dynamical quantum filtering in hydrogen-surface reactions. *Surf. Sci.* **418**, L39–L44 (1998).
4. Miura, Y., Kasai, H. & Diño, W. A. Dynamical quantum filtering in the scattering dynamics of H_2 on Cu(001). *J. Phys.: Condens. Matter* **14**, L479–L486 (2002).
5. Diño, W. A., Kasai, H. & Okiji, A. Dissociative Adsorption Dynamics of H_2 (D_2) on Metal Alloy Surfaces—A First Step Towards Surface Reaction Design/Control—. *J. Phys. Soc. Jpn.* **69**, 993–996 (2000).
6. Ogura, S. & Fukutani, K. Dynamic Blocking by CO of Hydrogen Transport across Pd_{70} Au_{30}(110) surfaces. *J. Phys. Chem. C* **121**, 3373–3380 (2017).
7. Namba, K. *et al*. Acceleration of hydrogen absorption by palladium through surface alloying with gold. *Proc. Nat. Acad. Sci.* **115**, 7896–7900 (2018).
8. Diño, W. A. Can we probe local surface reactivity with hydrogen molecules? *J. Phys.: Condens. Matter* **14**, 4379–4384 (2002).
9. Diño, W. A. *et al*. Probing Local Surface Reactivity with Hydrogen Molecules—Realizing an Atom/Molecule Scanning Probe—. *J. Vac. Soc. Jpn.* **46**, 391–396 (2003).
10. Barredo, D., Laurent, G., Nieto, P., Farías, D. & Miranda, R. High-resolution elastic and rotationally inelastic diffraction of D_2 from NiAl(110). *J. Chem. Phys.* **133**, 124702 (2010).
11. Nieto, P., Barredo, D., Farías, D. & Miranda, R. In-Plane and Out-of-Plane Diffraction of H_2 from Ru(001). *J. Phys. Chem. A* **115**, 7283–7290 (2011).
12. Farías, D. & Miranda, R. Diffraction of molecular hydrogen from metal surfaces. *Prog. Surf. Sci.* **86**, 222–254 (2011).
13. Hill, N. R. Quadrupole interaction in the scattering of H_2 from the surface of LiF: Rotational transitions. *Phys. Rev. B* **19**, 4269–4276 (1979).
14. Meyer, B., Padilla, J. & Vanderbilt, D. Theory of $PbTiO_3$, $BaTiO_3$, and $SrTiO_3$ surfaces. *Faraday Discuss.* **114**, 395–405 (1999).
15. Noguera, C. Polar oxide surfaces. *J. Phys.: Condens. Matter* **12**, R367–R410 (2000).
16. Piskunov, S., Heifets, E., Eglitis, R. & Borstel, G. Bulk properties and electronic structure of $SrTiO_3$, $BaTiO_3$, $PbTiO_3$ perovskites: an ab initio HF/DFT study. *Comp. Matter. Sci.* **29**, 165–178 (2004).
17. Wang, D., K., T., Ye, J. & Kimura, T. Photophysical and Photocatalytic Properties of $SrTiO_3$ Doped with Cr Cations on Different Sites. *J. Phys. Chem. B* **110**, 15824–15830 (2006).
18. Konta, R., Ishii, T., Kato, H. & Kudo, A. Photocatalytic Activities of Noble Metal Ion Doped $SrTiO_3$ under Visible Light Irradiation. *J. Phys. Chem. B* **108**, 8992–8995 (2004).
19. Jia, Q., Wu, X., Foltyn, S. & Tiwari, P. Structural and electrical properties of $Ba_{0.5}Sr_{0.5}TiO_3$ thin films with conductive $SrRuO_3$ bottom electrodes. *Appl. Phys. Lett.* **66**, 2197–2199 (1995).
20. Van der Berg, R., Blom, P., Cillessen, J. & Wolf, R. Field dependent permittivity in metal-semiconducting $SrTiO_3$ Schottky diodes. *Appl. Phys. Lett.* **66**, 697–699 (1995).
21. Tasker, P. W. The stability of ionic crystal surfaces. *J. Phys. C: Solid State Phys.* **12**, 4977–4984 (1979).
22. Kawasaki, M. *et al*. Atomic Control of the $SrTiO_3$ Crystal Surface. *Science* **266**, 1540–1542 (1994).
23. Aballe, L. *et al*. Instability and Surface Potential Modulation of Self-Patterned (001) $SrTiO_3$ Surfaces. *Chem. Mater.* **27**, 6198–6204 (2015).
24. Shimizu, K. *et al*. Molecular Adsorption, Hindered Rotation, and Species Separation of H_2/$SrTiO_3$(001). *J. Phys. Soc. Jpn.* **86**, 073601–1–4 (2017).
25. Sandler, Y. The Adsorption and Ortho-Para Conversion of Hydrogen on Diamagnetic Solids. II. The Relative Adsorbabilities of Orthohydrogen and Parahydrogen. *J. Phys. Chem.* **58**, 58–61 (1954).
26. Briquez, S. *et al*. Adsorption of ortho and para H_2 on NaCl(001). *J. Chem. Phys.* **109**, 6435–6449 (1998).
27. Silvera, I. F. & Nielsen, M. Inelastic Neutron Scattering and Separation Coefficient of Absorbed Hydrogen: Molecular Alignment and Energy Levels. *Phys. Rev. Lett.* **37**, 1275–1278 (1976).
28. Fukutani, K. & Sugimoto, T. Physisorption and ortho-para conversion of molecular hydrogen on solid surfaces. *Prog. Surf. Sci.* **88**, 279–348 (2013).
29. Sugimoto, T. & Fukutani, K. Effects of Rotational-Symmetry Breaking on Physisorption of Ortho- and Para-H_2 on Ag(111). *Phys. Rev. Lett.* **112**, 146101–1–5 (2014).
30. Ohno, S. *et al*. Rotational state modification and fast ortho-para conversion of H_2 trapped within the highly anisotropic potential of Pd(210). *Phys. Rev. B* **97**, 085436–1–5 (2018).
31. Diño, W. A., Kasai, H. & Okiji, A. Effects of Rotational State Excitations on the Dissociative Adsorption Dynamics of D_2/Cu(111). *J. Phys. Soc. Jpn.* **64**, 2478–2487 (1995).
32. Diño, W. A., Kasai, H. & Okiji, A. Role of Rotational Motion in the Dissociative Adsorption and Associative Desorption Dynamics of D_2 /Cu(111). *Phys. Rev. Lett.* **78**, 286–289 (1997).
33. Kroes, G.-J. & Mowrey, R. Scattering of H_2 by LiF(001) studied using a new model potential. I. Prediction of large differences in diffraction of cold beams of para-H_2 and normal-H_2. *J. Chem. Phys.* **103**, 2186–2201 (1995).
34. Bertino, M. F. *et al*. Observation of Large Differences in the Diffraction of Normal- and Para- H_2 from LiF(001). *Phys. Rev. Lett.* **81**, 5608–5611 (1998).
35. Lawless, W. N. Debye temperatures of ferroelectrics. *Phys. Rev. B* **17**, 1458–1459 (1978).
36. Kasai, H. & Okiji, A. Rotational Cooling and Vibrational Heating in Associative Desorption. *Prog. Theor. Phys. Suppl.* **106**, 341–348 (1991).
37. Kasai, H. & Okiji, A. Dynamics of vibrational excitation in molecule-surface interactions. *Prog. Surf. Sci.* **44**, 101–183 (1993).

38. Kasai, H., Brenig, W. & Müller, H. Rotational state distribution of NO molecules scattered from surfaces. *Z. Phys. B* **60**, 489–495 (1985).
39. Brenig, W., Kasai, H. & Müller, H. Coupled channel problems with Morse potentials: A simple and fast method. *Surf. Sci.* **161**, 608–626 (1985).
40. Brenig, W., Brunner, T., Groß, A. & Russ, R. Numerically stable solution of coupled channel equations: The local reflection matrix. *Z. Phys. B* **93**, 91–101 (1993).
41. Brenig, W. & Russ, R. Numerically stable solution of coupled-channel equations: the local transmission matrix. *Surf. Sci.* **315**, 195–203 (1994).
42. Brenig, W., Groß, A. & Russ, R. Numerically stable solution of coupled channel equations: the wave function. *Z. Phys. B* **97**, 311–317 (1995).
43. Kresse, G. & Furthmüller, J. Efficiency of ab-initio total energy calculations for metals and semiconductors using a plane-wave basis set. *Comput. Mater. Sci.* **6**, 15–50 (1996).
44. Kresse, G. & Furthmüller, J. Efficient iterative schemes for ab initio total-energy calculations using a plane-wave basis set. *Phys. Rev. B* **54**, 11169–11186 (1996).
45. Grimme, S. Semiempirical GGA-type density functional constructed with a long-range dispersion correction. *J. Comput. Chem.* **27**, 1787–1799 (2006).
46. Okazaki, A. & Kawaminami, M. Lattice constant of strontium titanate at low temperatures. *Mat. Res. Bull.* **8**, 545–550 (1973).
47. Momma, K. & Izumi, F. Vesta 3 for three-dimensional visualization of crystal, volumetric and morphology data. *J. Appl. Cryst.* **44**, 1272–1276 (2011).

Acknowledgements

This work is supported in part by MEXT Grants-in-Aid for Scientific Research (18H05518, 17K06818, 17H01057, 15H05736, 15KT0062, 15K14147, and 26248006); NEDO Project "R&D Towards Realizing an Innovative Energy Saving Hydrogen Society based on Quantum Dynamics Applications", Grants-in-Aid for JSPS Fellows; and Kawasaki Heavy Industries, Ltd. Some of the numerical calculations presented here done using the computer facilities at the following institutes: CMC (Osaka University), ISSP, KEK, NIFS, and YITP. Structure figures were plotted using the VESTA package[47].

Author contributions

K.S., W.A.D., H.N., K.F., and H.K. conceived the model and performed the calculation. All authors contributed to the discussion, analyses, and writing the manuscript.

Competing interests

A.Y. is an employee of Kawasaki Heavy Industries, Ltd. The other authors declare no competing interests.

Additional information

Correspondence and requests for materials should be addressed to W.A.D.

Reprints and permissions information is available at www.nature.com/reprints.

Publisher's note Springer Nature remains neutral with regard to jurisdictional claims in published maps and institutional affiliations.